ACS OMEGA

http://pubs.acs.org/journal/acsodf

Article

Improved Thermoelectric Performance of Monolayer HfS_2 by Strain Engineering

Hao Wang, Yang-Shun Lan, Bo Dai, Xiao-Wei Zhang, Zhi-Guo Wang, and Ni-Na Ge*

Cite This: *ACS Omega* 2021, 6, 29820–29829

Read Online

ACCESS | Metrics & More | Article Recommendations

ABSTRACT: Strain engineering can effectively improve the energy band degeneracy of two-dimensional transition metal dichalcogenides so that they exhibit good thermoelectric properties under strain. In this work, we have studied the phonon, electronic, thermal, and thermoelectric properties of 1T-phase monolayer HfS_2 with biaxial strain based on first-principles calculations combined with Boltzmann equations. At 0% strain, the results show that the lattice thermal conductivity of monolayer HfS_2 is 5.01 W m^{-1} K^{-1} and the electronic thermal conductivities of n-type and p-type doped monolayer HfS_2 are 2.94 and 0.39 W m^{-1} K^{-1}, respectively, when the doping concentration is around 5×10^{12} cm^{-2}. The power factors of the n-type and p-type doped monolayer HfS_2 are different, 29.4 and 1.6 mW mK^{-2}, respectively. Finally, the maximum ZT value of the n-type monolayer HfS_2 is 1.09, which is higher than 0.09 of the p-type monolayer HfS_2. Under biaxial strain, for n-type HfS_2, the lattice thermal conductivity, the electronic thermal conductivity, and the power factor are 1.55 W m^{-1} K^{-1}, 1.44 W m^{-1} K^{-1}, and 22.9 mW mK^{-2} at 6% strain, respectively. Based on the above factor, the ZT value reaches its maximum of 2.29 at 6% strain. For p-type HfS_2, the lattice thermal conductivity and the electronic thermal conductivity are 1.12 and 1.53 W m^{-1} K^{-1} at 7% strain, respectively. Moreover, the power factor is greatly improved to 29.5 mW mK^{-2}. Finally, the maximum ZT value of the p-type monolayer HfS_2 is 3.35 at 7% strain. It is obvious that strain can greatly improve the thermoelectric performance of monolayer HfS_2, especially for p-type HfS_2. We hope that the research results can provide data references for future experimental exploration.

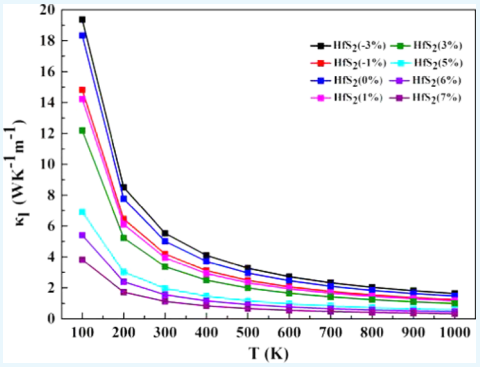

1. INTRODUCTION

In recent decades, as the energy crisis and environmental problems have become increasingly serious, researchers have begun to turn their attention to the development of high-efficiency energy.[1−3] Thermoelectric materials have great potential in waste-heat recovery, reduce greenhouse gas emissions, and provide cleaner forms of energy.[4] Thermoelectric devices not only have high application potential in aerospace components and household devices but can also be used in current integrated circuits to solve the problem of chip heat.[5−7] Thermoelectric material is a kind of functional material that can directly convert thermal energy into electrical energy by carrier movement in solids.[8,9] The performance of thermoelectric material is characterized by the dimensionless figure of merit, $ZT = S^2\sigma T/\kappa = S^2\sigma T/(\kappa_e + \kappa_l)$, where S is the Seebeck coefficient, σ is the electronic conductivity, T is the temperature, and κ is the thermal conductivity including both the electronic contribution (κ_e) and the lattice thermal conductivity (κ_l).[10] At present, the problem that hinders the large-scale application of thermoelectric materials is low thermoelectric conversion efficiency (low ZT value). However, it is very challenging to find suitable materials with large ZT since the transport coefficients (S, σ, κ) are interdependent quantities. Researchers found that band engineering,[11−13] nanostructural engineering,[14] and two-dimensional engineering[15] can help enhance the Seebeck coefficient and reduce the thermal conductivity, thereby effectively improving the thermoelectric properties of materials.

It has been discovered that various two-dimensional (2D) materials have higher thermoelectric ZT and also can be widely used in practical applications. Thus, 2D materials have attracted much attention due to their unique properties.[11,16−18] The main 2D thermoelectric materials are Group IV_A−VI_A compounds, black phosphorus (BP), nitrides, transition metal dichalcogenides (TMDCs), MXenes, and Xenes.[19−22] Among the various 2D materials, ZT can be effectively improved by selecting structural materials with lower thermal conductivity. For example, metal-shrouded semiconductor Tl_2O (group space $R\bar{3}m$) with a 1T structure has good thermoelectric properties due to its low thermal conductivity.[23] Likewise, TMDCs have also attracted much attention due to their relatively high

Received: August 10, 2021
Accepted: October 14, 2021
Published: October 26, 2021

electrical conductivity and relatively low thermal conductivity.[16,24] 2D TMDCs are divided into two kinds of crystal structures according to the arrangement of the atoms and the structures: trigonal prismatic (hexagonal, 2H-MoS_2 type) and octahedral (tetragonal, 1T-CdI_2 type). MoS_2 and WS_2 are typical TMDCs with a 2H-MoS_2 structure. Theoretical studies[25,26] indicated that the maximum ZT value of monolayer MoS_2 (monolayer WS_2) is 0.58 (0.067) at room temperature, which is mainly due to the high lattice thermal conductivity. Compared with the 2H-MoS_2 structure, the TMDC MX_2 (M = Zr, Hf; X = S, Se) with the 1T-CdI_2 structure has a much lower lattice thermal conductivity and a higher ZT value at room temperature.[27] For example, Bera et al. calculated that the ZT of monolayer HfS_2 (group space $P\bar{3}m1$) is 0.60,[28] and Singh et al. reported that the maximum ZT is 0.96.[29] Özbal et al. found that the ZT of TMDC HfS_2 with the 1T-CdI_2 structure reached 0.67 at room temperature and increased with increasing temperature.[24] This shows that HfS_2 with the 1T-CdI_2 structure is a kind of 2D thermoelectric material with good performance.

It is worth noting that the thermoelectric properties of materials are greatly affected by strain in practical applications. For example, the strain-induced band degeneracy improves the electronic transport properties, and the phonon dispersion distortion may decrease κ_l, both of which result in the enhancement of ZT.[26,30] In this paper, first-principles calculations combined with the Boltzmann transport equation are used to calculate the thermoelectric properties of monolayer HfS_2 at different strains (the strain range from −3 to 7%; negative numbers represent compressive and positive numbers represent tensile strain). This not only enriches the research content of 1T-CdI_2 monolayer HfS_2 thermoelectric performance but also effectively predicts the changing trend of the thermoelectric properties of monolayer HfS_2 under strain. We hope the research results have importance for guiding the improvement of material processing in the future.

2. COMPUTATIONAL METHODS

The structural optimization of unstrained and strained monolayer HfS_2 with the 1T-CdI_2 structure (as shown in Figure 1) in the Vienna ab initio simulation package (VASP) is performed using generalized gradient approximation (GGA) within Perdew−Burke−Ernzerhof (PBE) formulation exchange−correlation interaction on the basis of density functional theory.[31−33] The plane-wave energy cutoff is chosen as 500 eV, and the Monkhorst−Pack k mesh is 13 × 13 × 1. Geometrical structures were relaxed until the force on each atom was less than 0.001 eV·Å^{-1}. To avoid interaction with periodic images, a 15 Å thick vacuum slab is added in the direction of the vertical two-dimensional plane.

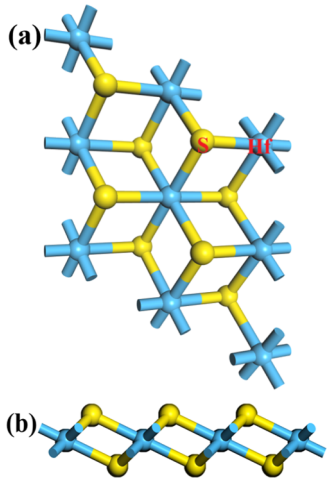

Figure 1. (a) Top and (b) side views of monolayer HfS_2 in the 1T-CdI_2 type, where the blue and yellow balls represent the Hf and S atoms, respectively.

To obtain lattice thermal transport, we solved the Boltzmann equation for phonon as implemented in ShengBTE.[34] The Phonopy code was used to obtain the phonon dispersions and second-order interatomic force constants (IFCs).[35] The third-order interatomic force constants are extracted from ShengBTE. The second-order and third-order interatomic force constants were calculated using a 3 × 3 × 1 supercell with 5 × 5 × 1 k meshes based on the relaxed unit cell. The lattice thermal conductivity of monolayer HfS_2 requires the conversion of the following formula from the results obtained by ShengBTE

$$\kappa_{\alpha\beta} = \frac{1}{SH}\sum_{\lambda} C_{\lambda}\nu_{\lambda\alpha}\nu_{\lambda\beta}\tau_{\lambda} \quad (1)$$

where S is the surface area; H is determined by $H_{HfS_2} = h_{HfS_2} + 2r_S$, where h_{HfS_2} is the height difference of the top and the bottom S atom; and r_S is the van der Waals radii of the S atom.[36,37]

The electronic thermal conductivity was calculated using the Wiedemann−Franz law

$$\kappa_e = L\sigma T \quad (2)$$

where L is the Lorenz number, and in this work, we use $L = 2.45 \times 10^{-8}$ J^2 K^{-2} C^{-2}.[10]

For the calculations of the Seebeck coefficient and the electrical conductivity over relaxation time (σ/τ), we use the electron Boltzmann transport theory within relaxation time approximation (RTA) as implemented in the BoltzTrap software package.[38] To obtain accurate transport properties, a large 51 × 51 × 1 k-point Monkhorst−Pack mesh is used to calculate the band energies. Finally, the relaxation time (τ) is estimated using the Bardeen−Shockley deformation potential theory based on the effective mass approximation

$$\tau = \frac{\mu m^*}{e} \quad (3)$$

$$\mu = \frac{e\hbar^3 C_{2d}}{k_B T m^* m_d E_l^2} \quad (4)$$

where μ, C_{2D}, and E_l are the carrier mobility, the effective elastic modulus, and the deformation potential constant, respectively; $m^* = \hbar^2[\partial^2 E/\partial k^2]^{-1}$ is the effective mass of the carrier; and $m_d = \sqrt{m_x^* m_y^*}$ is the average effective mass.[39,40]

3. RESULTS AND DISCUSSION

3.1. Thermoelectric Properties of Unstrained Monolayer HfS_2. Table 1 shows the stable crystal structure of monolayer HfS_2, which can be observed to be in good agreement with the theoretical results in previous reports in the literature[28,41−43] and proves the reliability of our calculations. Furthermore, the stability of the structure is verified by calculating the phonon dispersion without an imaginary frequency (Figure 2a). Finally, the trend graph of lattice thermal conductivity with temperature is obtained (Figure 2b). Moreover, the κ_l of monolayer HfS_2 is 5.01 W m^{-1} K^{-1} at 300 K. This

https://doi.org/10.1021/acsomega.1c04286
ACS Omega 2021, 6, 29820−29829

Table 1. Lattice Constants (Å) from PBE Calculations and Those in the Literature

	method	lattice constant
HfS_2	expt (bulk)	3.631[28]
	PBE	3.65[41]
	PBE	3.643 (present)
	PBE	3.674[42]
	PBEsol	3.64[43]

is indeed lower than the 8.77 W m^{-1} K^{-1} reported in a previous report in the literature for bulk HfS_2,[44] but the results obtained are higher than the κ_l of monolayer HfS_2, 2.836 W m^{-1} K^{-1}, as reported by Bera et al. and 0.71 W m^{-1} K^{-1} as reported by Özbal et al.[24,28] It is worth pointing out that monolayer HfS_2 has a much smaller κ_l compared with MoS_2 and WS_2 monolayers.[45−47]

Figure 3a,b shows the band structure of the monolayer HfS_2 by the PBE functional, HSE hybrid functional, and the SOC effect. The band gaps predicted by the HSE hybrid functional and the SOC effect are 2.13 and 1.17 eV, respectively, while the band gap predicted by the PBE functional is 1.31 eV. It is found that the band gap predicted by the PBE functional is basically consistent with the theoretical results (1.30 and 1.29 eV)[24,28] and the latest experiment of HfS_2 nanosheets (1.30 eV).[48] Therefore, for monolayer HfS_2, the PBE functional is used as a calculation method in subsequent research calculations.

The electronic transport coefficients (Seebeck coefficient, electrical conductivity over relaxation time, power factor over relaxation time ($S^2\sigma/\tau$)) and the electronic thermal conductivity over relaxation time (κ_e/τ) in the range of $0.01-10 \times 10^{13}$ cm^{-2} doping concentration are shown in Figure 4a−d. In Figure 4a, we show the calculated σ/τ as a function of doping concentration for monolayer HfS_2. It was shown that the σ/τ of p-type doping is slightly larger than that of n-type doping within a range of doping concentrations less than 7×10^{13} cm^{-2}. When the doping concentration is higher than 7×10^{13} cm^{-2}, the σ/τ of n-type doping is larger than that of p-type doping. In Figure 4b, we show the calculated Seebeck coefficient as a function of doping concentration for monolayer HfS_2. We observe that the value of the Seebeck coefficient decreases first and then increases slightly with an increase of doping concentration, and the Seebeck coefficient of n-type doping is larger than that of p-type doping.

In Figure 4c, we show the calculated $S^2\sigma/\tau$ as a function of doping concentration for monolayer HfS_2. The $S^2\sigma/\tau$ of n-type doping is larger than that of p-type doping, and with an increase of doping concentration, the difference increases gradually, which indicates that the changing trend of $S^2\sigma/\tau$ is mainly related to the change of the Seebeck coefficient. Then, we calculate the κ_e/τ. As can be seen from Figure 4d, the κ_e/τ of n-type doping exceeds that of p-type doping at high carrier concentrations.

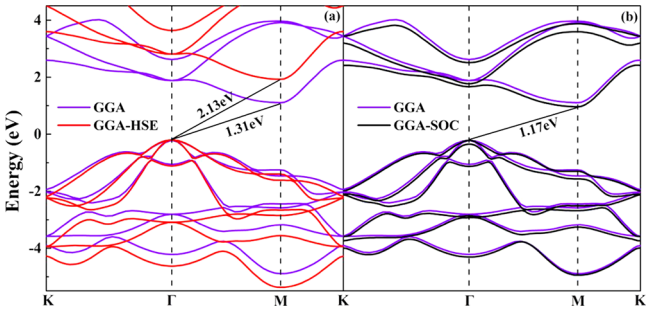

Figure 3. Band structure of monolayer HfS_2 calculated by (a) HSE hybrid functional and (b) SOC effect with a comparison to the PBE functional.

To obtain ZT, we must first calculate the relaxation time, as shown in eqs 3 and 4. The specific parameters and results are shown in Table 2. Under 0% strain, in the vicinity of the optimum doping concentration of 5×10^{12} cm^{-2}, we obtained the power factor and thermal conductivity ($\kappa_e + \kappa_l$) of n-type doping and p-type doping. The power factors are 29.4 and 1.6 mW mK^{-2}, and the thermal conductivities are 7.95 and 5.5 W m^{-1} K^{-1}, respectively. The results show that the power factor of n-type doping is much greater than that of p-type doping, and the thermal conductivity difference between n-type and p-type doping is not particularly large. Based on this, we can roughly predict that the maximum value of ZT for n-type should be higher than that for p-type. Finally, the ZT for unstrained monolayer HfS_2 can be determined. At 300 K, the maximum value of ZT for p-type is 0.09, and that for n-type is 1.09. The calculated ZT as a function of carrier concentrations is shown in Figure 5. That is, the thermoelectric properties of n-type doping are better than those of p-type doping for monolayer HfS_2 at 0% strain. Our calculated ZT for p-type is consistent with previous reports in the literature, 0.13 and 0.26;[28] however, that for n-type is slightly higher than the reported data, 0.6 and 0.67,[24] but is more consistent with 0.96.[29]

3.2. Thermoelectric Properties of Strained Monolayer HfS_2. A series of in-plane biaxial strains, including compressive and tensile strain, are applied to monolayer HfS_2 and are defined as

$$\varepsilon = (a - a_0)/a_0 \times 100\% \quad (5)$$

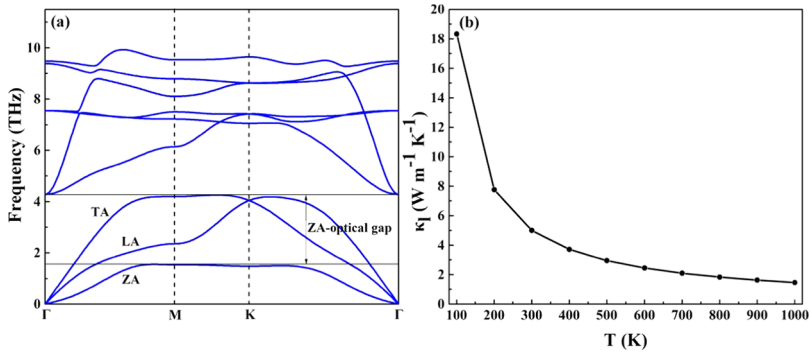

Figure 2. (a) Phonon spectra of monolayer HfS_2 and (b) the temperature dependence of lattice thermal conductivity of monolayer HfS_2.

https://doi.org/10.1021/acsomega.1c04286
ACS Omega 2021, 6, 29820−29829

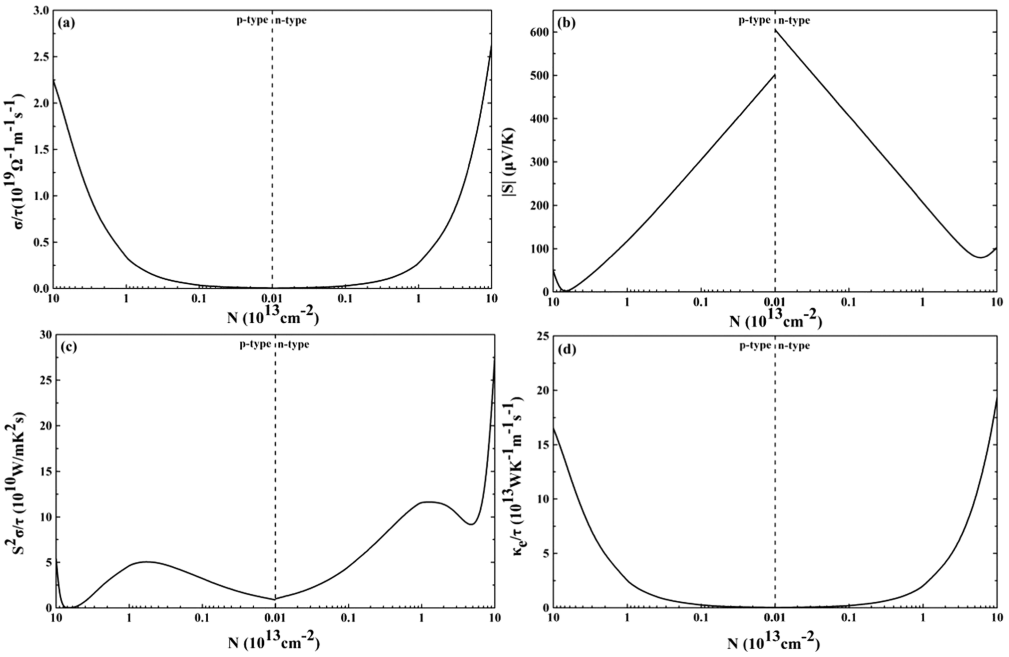

Figure 4. Calculated electronic transport coefficients ((a) σ/τ, (b) S, (c) $S_2\sigma/\tau$, and (d) κ_e/τ) as a function of carrier concentration for both p-type and n-type monolayer HfS_2.

Table 2. Effective Mass (m^*), Average Effective Mass (m_d), Elastic Modulus (C_{2D}), Deformation Potential Constant (E_l), Electron and Hole Mobility (μ), and Relaxation Time (τ) of Monolayer HfS_2

carrier type		m^* (m_0)	m_d (m_0)	C_{2D} (N m^{-1})	E_l (eV)	μ (cm^{-2} V^{-1} s^{-1})	τ (10^{-14} s)
electron	HfS_2	1.43	4.62	202.72	1.37	364.2	29.7
hole	HfS_2	1.44	0.44	202.72	13.3	38.2	3.1

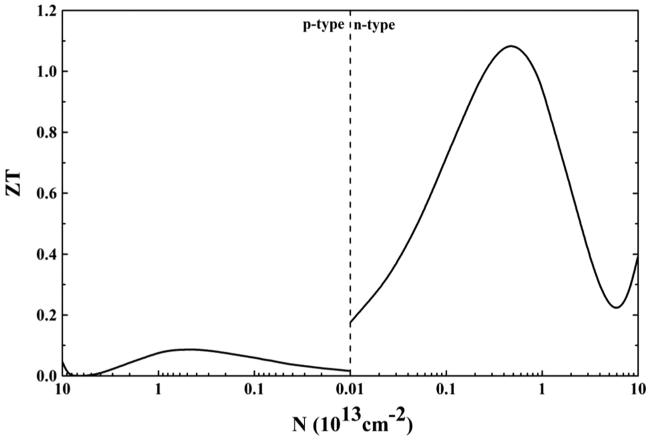

Figure 5. Calculated ZT as a function of carrier concentration for both p-type and n-type monolayer HfS_2.

where a_0 and a are the unstrained and strained cell parameters, respectively. Biaxial strains ranging from −6 to 10% were considered. There is an imaginary frequency mode in the phonon spectrum of monolayer HfS_2 in the high symmetry directions under strains of −6 and 10%. Therefore, only the results of −3, −1, 0, 1, 3, 5, 6, and 7% biaxial strains are given as representative cases. The corresponding phonon spectra are shown in Figure 6a−h. There is no imaginary frequency mode in the phonon spectrum of monolayer HfS_2 in the high symmetry directions under strain ranging from −3 to 7%. It is proved that the structure is stable under seven kinds of strain.

According to previous reports,[44] the ZA phonon is the main heat conduction carrier in HfS_2, and the ZA optical gap determines the intensity of the scattering. If the ZA optical gap is smaller, the scattering between the ZA modes and optical modes is stronger, which may result in a smaller lattice thermal conductivity.[44] With the increase of biaxial strain from −3 to 7%, the ZA optical gap decreases. It is reasonable to predict that the lattice thermal conductivity decreases with an increase of biaxial strain from −3 to 7%. Finally, as can be seen from Figure 7, the trend of the lattice thermal conductivity is almost consistent with our previous predictions as the biaxial strain changes from −3 to 7%.

It is worth noting that we observe a large change in the lattice thermal conductivity when the strain reaches 5% and above. Therefore, we explain this phenomenon by analyzing the changes in phonon group velocity and relaxation times from Figure 8. From Figure 8a−d, the group velocity of acoustic modes is basically larger than that of the optical modes, and only the group velocity of the optical modes between 4 and 8 THz is greater than that of the acoustic modes. When the strain reaches 5% and more, the group velocity of the acoustic modes is significantly reduced, while the group velocity of the optical modes increases. Regardless of the acoustic mode or the optical mode, their frequencies decrease. Mode-dependent phonon relaxation times for ZA, LA, TA, and optical modes under different biaxial strains are shown in Figure 8e−h. The ZA, LA, TA modes have larger relaxation times than the optical modes, which indicates that the phonon scattering rate of the acoustic modes is lower than that of the optical modes. This also shows that the acoustic mode has a greater contribution to the thermal

https://doi.org/10.1021/acsomega.1c04286
ACS Omega 2021, 6, 29820−29829

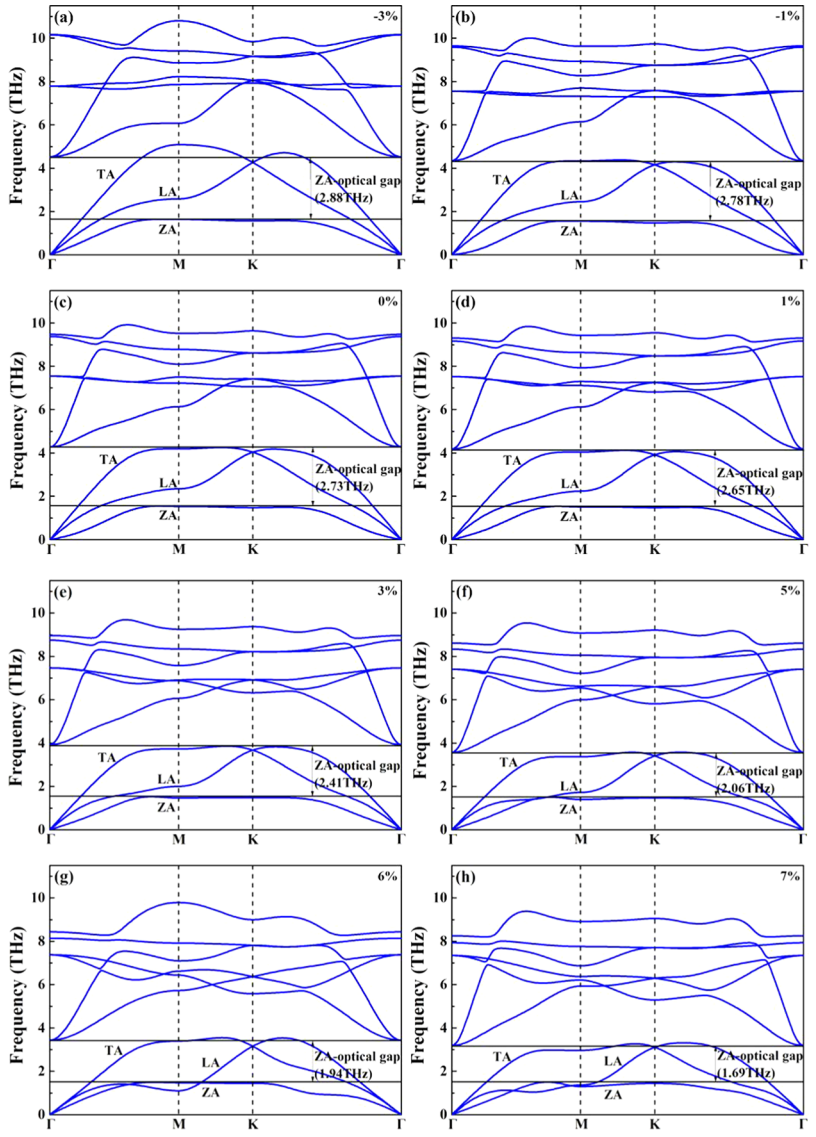

Figure 6. Calculated phonon spectra of the monolayer HfS_2 under different biaxial strains: (a) −3%, (b) −1%, (c) 0%, (d) 1%, (e) 3%, (f) 5%, (g) 6%, and (h) 7%.

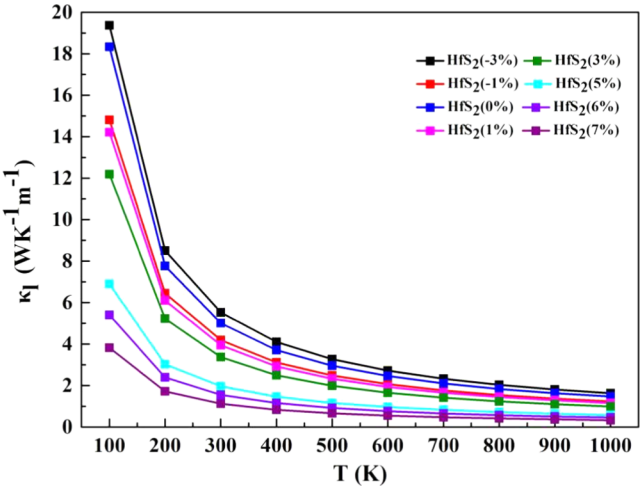

Figure 7. Calculated lattice thermal conductivity of monolayer HfS_2 as a function of carrier concentration at different biaxial strains.

conductivity of the lattice than the optical mode. But regardless of the acoustic mode or the optical mode, their relaxation times are significantly reduced when the strain reaches 5% and more. This shows that the phonon scattering rate increases significantly when the strain reaches 5% and more. The high phonon scattering rate and low phonon group velocity also cause the lattice thermal conductivity to reduce significantly when the strain reaches 5%.

The calculated electronic structures of monolayer HfS_2 under different strains are shown in Figure 9a–h. It is well-known that strain can modify the band structure. In this paper, we found that the tensile strain led to an increase in the band gap and a compressive strain led to a decrease in the band gap. When the biaxial stress effect is from −3 to 7%, the band gap of the system increases from 0.9 to 1.83 eV. Furthermore, the energy difference between valleys I and II (III and IV) is denoted as ΔC (ΔV), namely, $\Delta C = E_I - E_{II}$, $\Delta V = E_{IV} - E_{III}$, where E_I and E_{II} denote the two conduction band valleys near the Fermi level, and E_{III}, E_{IV}, and E_V denote the three valence band valleys near the Fermi level. It is theoretically considered that ΔV less than a certain value (compared with k_BT, where k_B is the Boltzmann

https://doi.org/10.1021/acsomega.1c04286
ACS Omega 2021, 6, 29820−29829

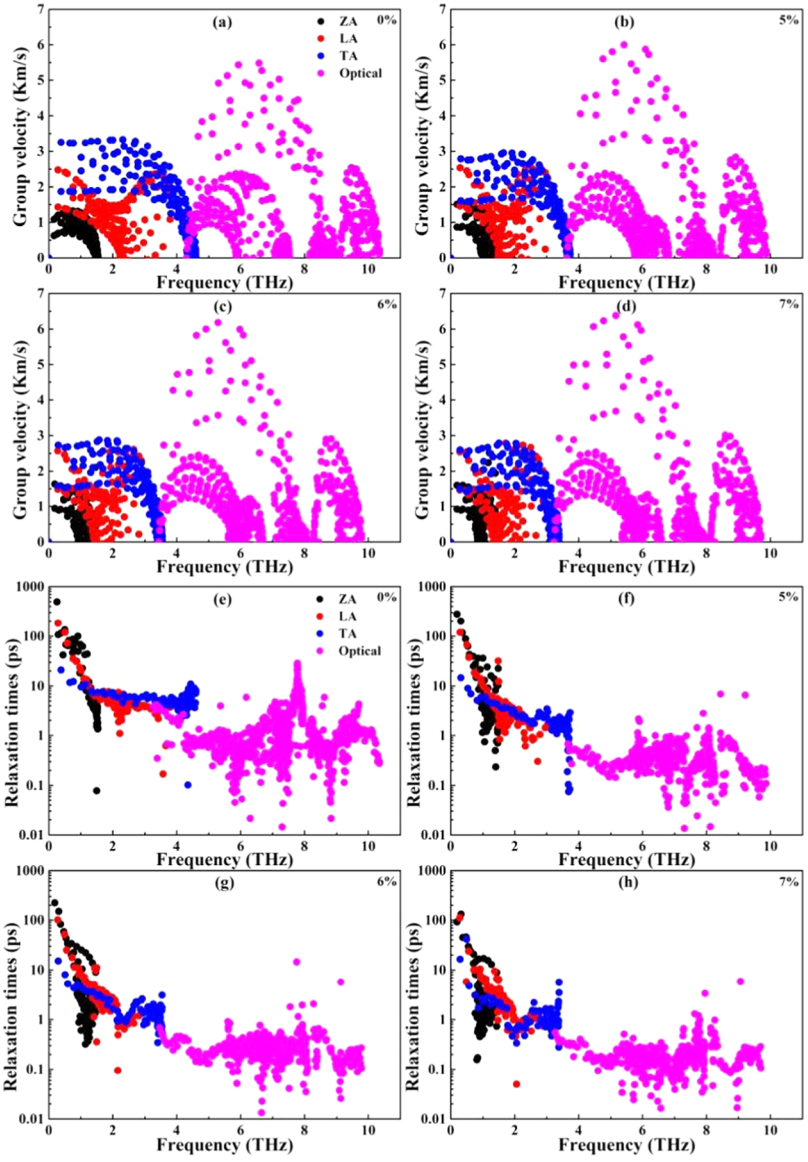

Figure 8. Magnitude of the phonon group velocity as a function of frequency in the full BZ under different biaxial strains: (a) 0%, (b) 5%, (c) 6%, and (d) 7%. Mode-dependent phonon relaxation times for ZA, LA, TA, and optical modes under different biaxial strains: (e) 0%, (f) 5%, (g) 6%, and (h) 7%.

constant) represents the merging of energy levels[3,5,11,13,30] and affects the thermoelectric properties of the material. The increase of the degeneracy in the valley is generally helpful to improve the thermoelectric properties of thermoelectric materials.[5,26,30] This is because the multiple degenerate valleys increase the effective mass without significantly decreasing the carrier mobility.[26] As can be seen from Figure 10a, ΔV decreases with increasing strain and approaches 0 eV at 5% strain. This shows that the three valleys of the valence band can be regarded as being effectively converged. In other words, the energy levels are merged.

Under the action of strain, the lattice constant of the crystal structure changed and the position of the atom also shifted, resulting in a change in the characteristics and strength of the bond between atoms so that the band structure changed. This can also be observed from the information in Figure 10b of the partial density of states (PDOS) of monolayer HfS_2. The PDOSs at 0, 5, and 7% strains are calculated and compared as shown in Figure 10b. It can be seen from Figure 10b that the valance band is mainly contributed by the 3p orbital of the S atom, and in the range of energy level from 0 to −1 eV, the PDOS at 5% strain is obviously greater than the PDOS at 0 and 7% strains. Therefore, when the biaxial strain is at around 5%, the band of the monolayer HfS_2 converges. Finally, the Seebeck coefficient and the power factor of p-type doping may be the highest at 5% strain. In the following, it is shown that the Seebeck coefficient and the power factor are indeed the largest under the stress of 5%, as shown in Figure 11b,c.

The electron transport coefficients under different strains were calculated on the basis of the semiclassical Boltzmann theory. Figure 11a shows the variation of σ/τ with carrier concentration under different strains. The σ/τ increases with increasing carrier concentration. When the biaxial strain changes from −3 to 7%, the σ/τ decreases, and the p-type conductance varies greatly with strain, while the n-type conductance varies little with strain. Moreover, we find that the σ/τ of n-type is obviously higher than that of p-type under the same conditions.

https://doi.org/10.1021/acsomega.1c04286
ACS Omega 2021, 6, 29820−29829

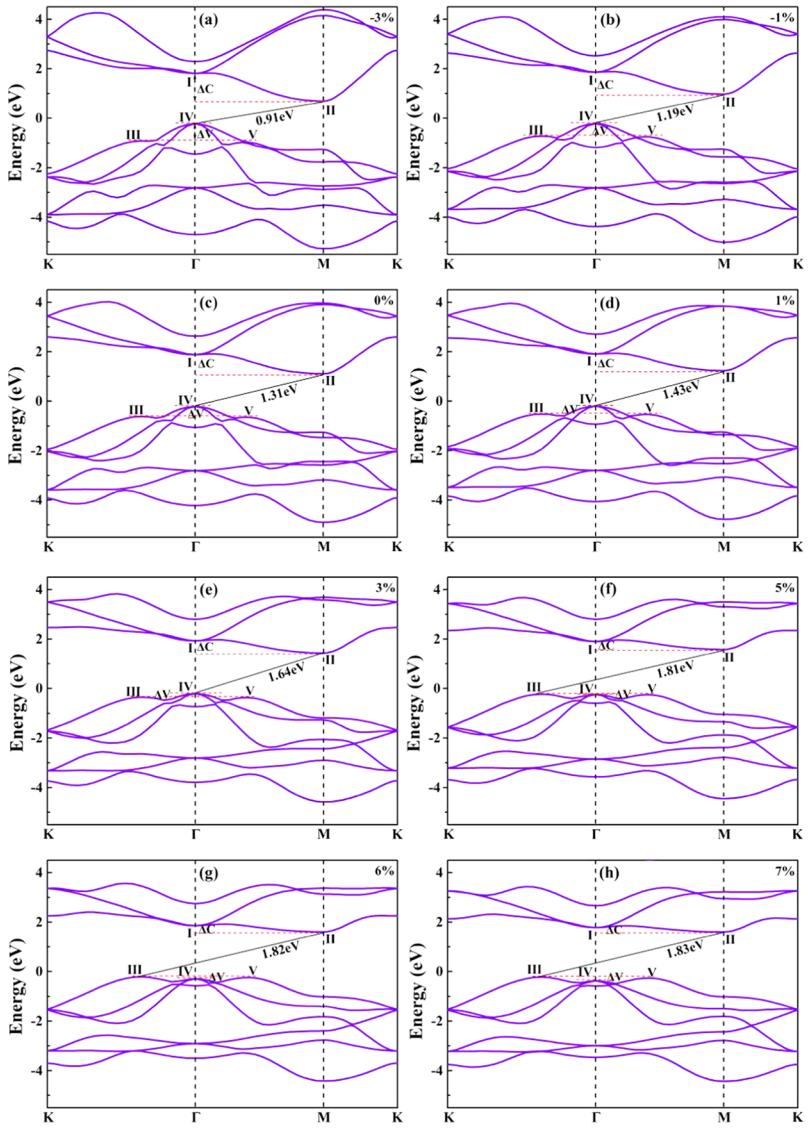

Figure 9. Band structure of monolayer HfS_2 under different biaxial strains: (a) −3%, (b) −1%, (c) 0%, (d) 1%, (e) 3%, (f) 5%, (g) 6%, and (h) 7%. The two conduction band valleys near the Fermi level (0 eV) are denoted by I and II. The three valence band valleys near the Fermi level are denoted by III, IV, and V. ΔC (ΔV) represents the energy difference between I and II (III and IV).

Figure 11b shows the variation of S with carrier concentration under different strains. The overall trend of S decreases with increasing carrier concentration. For p-type doping, we find that S increases with the increasing biaxial strain and becomes maximum at a strain of 5%. For n-type doping, S increases when the strain changes from −3 to 7%. Figure 11c shows the variation of $S^2\sigma/\tau$ with carrier concentration under different strains. For p-type doping, $S^2\sigma/\tau$ increases with the increasing strain and reaches the maximum value under 5% strain. For n-type doping, $S^2\sigma/\tau$ increases monotonically with the increasing strain and reaches the maximum value under 7% strain. As mentioned above, the increase of the degeneracy in the valance band valley is in favor of the increase of S and $S^2\sigma/\tau$; that is to say, the increase of S and $S^2\sigma/\tau$ is accompanied by the decrease of ΔC under strain from −3 to 7%, which is consistent with our results (Figure 11). Now, we have the ratio of the electronic transport coefficients and the relaxation time, and the effect of relaxation time cannot be ignored.

Figure 11d shows the variation of κ_e/τ with carrier concentration under different strains. For both n-type and p-type doping, we find that κ_e/τ decreases with the increase of strain from −3 to 7%, and the κ_e/τ of p-type doping is obviously smaller than that of n-type doping, especially when the strain is below 3%.

Table 3 shows the effective mass, average effective mass, elastic modulus, deformation potential constant, and relaxation time of monolayer HfS_2 at −3, −1, 0, 1, 3, 5, 6, and 7% biaxial strains.

Combining all of the calculated coefficients together, the variation of the ZT value with carrier concentration is shown in Figure 12. The ZT value of p-type doping is only 0.09 at 0% strain. Moreover, we find that the ZT value of p-type doping changes greatly with the increase of strain. When the strain increases to 7%, the ZT value reaches 3.35, with a huge improvement. The ZT value of n-type doping is 1.09 at 0% strain, which is much higher than that of p-type doping. On further applying strain to it and on reaching 6% strain, we find that the ZT value further increased to 2.29. Under biaxial strain, we find that the ZT value of p-type doping exceeds that of n-type doping when the strains are at 6 and 7%. The reason for this can

https://doi.org/10.1021/acsomega.1c04286
ACS Omega 2021, 6, 29820−29829

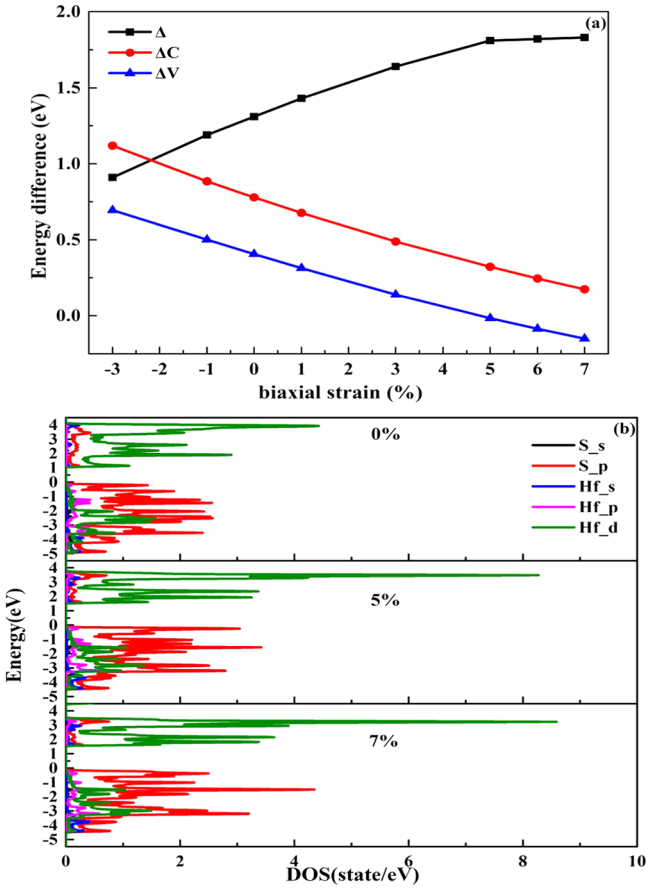

Figure 10. (a) Band gaps (Δ) and the energy difference between the conduction and valance band valleys (Δ*C* and Δ*V*, respectively) as a function of the applied biaxial strain. (b) Partial density of states of the monolayer HfS_2 at 0, 5, and 7% strains.

be seen from Table 3; the relaxation time of p-type doping is larger than that of n-type doping, and the difference between the $S^2\sigma/\tau$ of p-type and n-type doping is not significant. Therefore, the $S^2\sigma$ of p-type doping is higher than that of n-type doping. For p-type, the power factor is 35.5 mW mK^{-2} at 6% strain with the hole concentration at 6×10^{12} cm^{-2} and the power factor is 29.5 mW mK^{-2} at 7% strain with the hole concentration at 5×10^{12} cm^{-2}. For n-type, the power factor is 22.9 mW mK^{-2} at 6% strain with the electron concentration at 4×10^{12} cm^{-2} and the power factor is 12.3 mW mK^{-2} at 7% strain with the electron concentration at 6×10^{12} cm^{-2}. In addition, we also obtained the thermal conductivity at 6 and 7% strains. At 6% strain, the thermal conductivity of p-type and n-type doping are 3.37 and 2.99 W m^{-1} K^{-1}, respectively. The thermal conductivities of p-type and n-type doping are 2.65 and 2.01 W m^{-1} K^{-1}, respectively, at 7% strain. We infer from this result that the thermal conductivity differences for both n-type and p-type doped monolayer HfS_2 are not particularly large. Therefore, the *ZT* value of p-type doping is ultimately greater than that of n-type doping at 6 and 7% strains. It can be seen that the strain in a certain range can simultaneously increase *S* and the power factor and can also reduce the thermal conductivity. The combined effect of these factors ultimately improves their thermoelectric performance.

4. CONCLUSIONS

We have studied the phonon, electronic, thermal, and thermoelectric properties of monolayer HfS_2 with and without biaxial strain based on first-principles calculations combined with Boltzmann equations. At 0% strain, the results show that the *ZT* value of n-type HfS_2 at the optimal doping concentration is 1.09, while the *ZT* value of p-type HfS_2 is only 0.09. This indicates that the thermoelectric performance of n-type HfS_2 is much higher than that of p-type HfS_2 under the condition of 0% strain. Moreover, the strain can effectively improve the thermoelectric properties of materials. For n-type, the maximum *ZT* value is 2.29 at 6% strain, and for p-type, the maximum *ZT* value is 3.35 at 7% strain. This indicates that strain can greatly improve the thermoelectric performance of single-layer HfS_2, especially for p-type HfS_2.

At the same time, we can also see that when the strain reaches 5%, the energy level degeneracy is the strongest, resulting in the rapid increase of *ZT* values for p- and n-type HfS_2. That is to say,

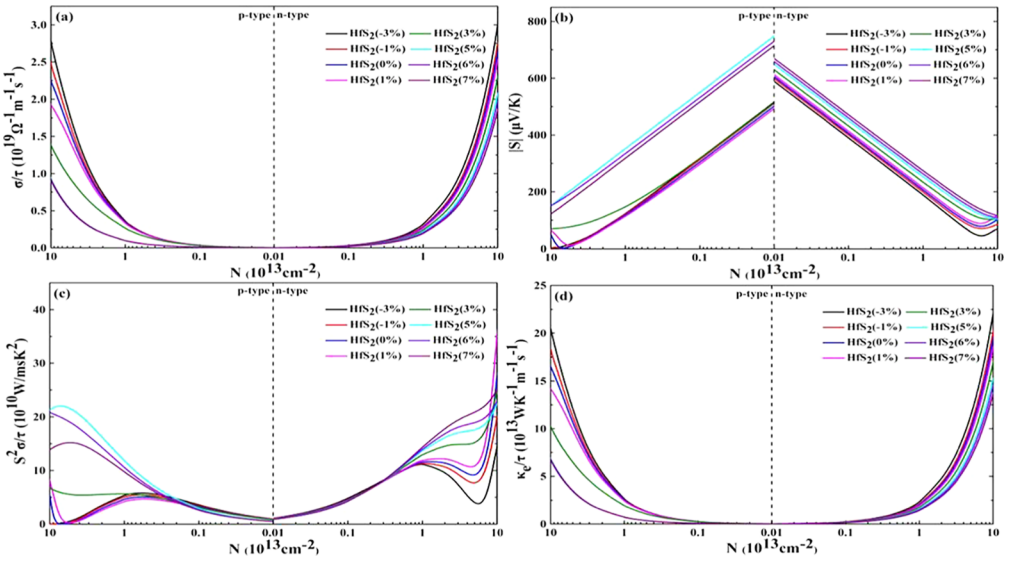

Figure 11. Calculated electronic transport coefficients ((a) σ/τ, (b) *S*, (c) $S^2\sigma/\tau$, and (d) κ_e/τ) as a function of carrier concentration for both p-type and n-type monolayer HfS_2 at different biaxial strains.

https://doi.org/10.1021/acsomega.1c04286
ACS Omega 2021, 6, 29820−29829

Table 3. Effective Mass (m^*), Average Effective Mass (m_d), Elastic Modulus (C_{2D}), Deformation Potential Constant (E_l), Electron and Hole Mobility (μ), and Relaxation Time (τ) of Monolayer HfS_2 at −3, −1, 0, 1, 3, 5, 6, and 7% Biaxial Strains

carrier type		m^* (m_0)	m_d (m_0)	C_{2D} (N m^{-1})	E_l (eV)	μ (cm^{-2} V^{-1} s^{-1})	τ (10^{-14} s)
electron	strained (−3%)	1.29	4.07	247.49	1.20	733.5	53.9
	strained (−1%)	1.38	4.41	218.00	1.15	607.0	47.7
	strained (0%)	1.43	4.62	202.72	1.37	364.2	29.7
	strained (1%)	1.41	4.83	187.04	1.14	450.6	36.2
	strained (3%)	1.58	5.37	167.31	1.13	346.1	31.1
	strained (5%)	1.70	6.12	146.21	1.07	275.1	26.6
	strained (6%)	1.76	6.62	135.36	1.01	243.0	24.3
	strained (7%)	1.82	7.20	130.24	1.47	103.1	10.7
hole	strained (−3%)	1.45	0.44	247.49	15.4	35	2.89
	strained (−1%)	1.45	0.46	218.00	13.9	36.2	2.99
	strained (0%)	1.44	0.44	202.72	13.3	38.2	3.10
	strained (1%)	1.45	0.48	187.04	12.5	37.5	3.00
	strained (3%)	1.45	0.50	167.31	10.9	43.4	3.58
	strained (5%)	1.97	0.87	146.21	4.53	88.7	9.95
	strained (6%)	1.93	0.86	135.36	2.09	398.4	43.8
	strained (7%)	1.90	0.86	130.24	2.08	393.1	42.5

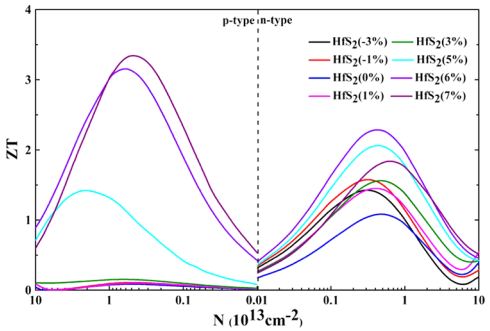

Figure 12. Calculated *ZT* as a function of carrier concentration for both p-type and n-type monolayer HfS_2 at different biaxial strains.

the thermoelectric properties of monolayer HfS_2 can be effectively enhanced by band valley engineering. It is hoped that our work can supplement and improve the two-dimensional thermoelectric material database, providing suggestions for future new material design.

AUTHOR INFORMATION

Corresponding Author

Ni-Na Ge − *State Key Laboratory of Environment-friendly Energy Materials, Southwest University of Science and Technology, Mianyang 621010, China;* orcid.org/0000-0002-4237-839X; Email: genina911@163.com

Authors

Hao Wang − *State Key Laboratory of Environment-friendly Energy Materials, Southwest University of Science and Technology, Mianyang 621010, China*

Yang-Shun Lan − *College of Physical Science and Technology, Sichuan University, Chengdu 610065, China*

Bo Dai − *State Key Laboratory of Environment-friendly Energy Materials, Southwest University of Science and Technology, Mianyang 621010, China*

Xiao-Wei Zhang − *State Key Laboratory of Environment-friendly Energy Materials, Southwest University of Science and Technology, Mianyang 621010, China*

Zhi-Guo Wang − *University of Electronic Science and Technology of China, Chengdu 610054, China;* orcid.org/0000-0002-5652-5362

Complete contact information is available at: https://pubs.acs.org/10.1021/acsomega.1c04286

Notes

The authors declare no competing financial interest.

ACKNOWLEDGMENTS

The authors acknowledge the National Natural Science Foundation of China (Nos. 11504304 and 11972313) and the Project of State Key Laboratory of Environment-friendly Energy Materials, Southwest University of Science and Technology (Nos. 19fksy07 and 20fksy23) for the funding. They also thank Dr. Lei Liu (Southwest University of Science and Technology, Mianyang, Sichuan 610064, China) for guidance.

REFERENCES

(1) Chen, Z. G.; Han, G.; Yang, L.; Cheng, L.; Zou, J. Nanostructured thermoelectric materials:current research and future challenge. *Prog. Nat. Sci.: Mater. Int.* **2012**, *22*, 535−549.

(2) Lan, Y. S.; Chen, X. R.; Hu, C. E.; Cheng, Y.; Chen, Q. F. Penta-PdX_2 (X = S, Se, Te) monolayers: promising anisotropic thermoelectric materials. *J. Mater. Chem. A* **2019**, *7*, 11134−11142.

(3) Tan, G.; Zhao, L. D.; Kanatzidis, M. G. Rationally designing high-performance bulk thermoelectric materials. *Chem. Rev.* **2016**, *116*, 12123−12149.

(4) Martín-González, M.; Caballero-Calero, O.; Díza-Chao, P. Nanoengineering thermoelectrics for 21st century: Energy harvesting and other trends in the field. *Renewable Sustainable Energy Rev.* **2013**, *24*, 288−305.

(5) Pei, Y.; Wang, H.; Snyder, G. Band engineering of thermoelectric materials. *Adv. Mater.* **2012**, *24*, 6125−6135.

(6) Li, J. F.; Liu, W. S.; Zhao, L. D.; Zhou, M. High-performance nanostructured thermoelectric materials. *NPG Asia Mater.* **2010**, *2*, 152−158.

(7) Abdollah, H. M.; Mohammad, Y.; Mojtaba, Y.; Alireza, A. Investigation into thermoelectric properties of M (M = Hf, Zr) X_2 (X = S, Se, Te) nanotubes using first-principle calculations. *Solid State Commun.* **2021**, *336*, No. 114289.

(8) Zhao, L. D.; Lo, S. H.; Zhang, Y.; Sun, H.; Tan, G.; Uher, C.; Wolverton, C.; Dravid, V. P.; Kanatzidis, M. G. Ultralow thermal conductivity and high thermoelectric figure of merit in SnSe crystals. *Nature* **2014**, *508*, 373−377.

(9) Vineis, C. J.; Shakouri, A.; Majumdar, A.; Kanatzidis, M. G. Nanostructured thermoelectircs: Big efficiency gains from small features. *Adv. Mater.* **2010**, *22*, 3970−3980.

(10) Yan, P.; Gao, G. Y.; Ding, G. Q.; Qin, D. Bilayer MSe_2 (M = Zr, Hf) as promising two-dimensional thermoelectric materials: a first-principles study. *RSC Adv.* **2019**, *9*, 12394−12403.
(11) Pei, Y.; Shi, X.; Lalonde, A.; Wang, H.; Chen, L.; Snyder, G. J. Convergence of electronic bands for high performance bulk thermoelectrics. *Nature* **2011**, *473*, 66−69.
(12) Fang, T.; Zheng, S.; Zhou, T.; Yan, L.; Zhang, P. Computational prediction of high thermoelectric performance in p-type half-heusler compounds with low band effective mass. *Phys. Chem. Chem. Phys.* **2017**, *19*, 4411−4417.
(13) Zhu, T.; Lin, Y.; Fu, C.; Heremans, J. P.; Snyder, J. G.; Zhao, X. Compromise and synergy in high-efficiency thermoelectric materials. *Adv. Mater.* **2017**, *29*, No. 1605884.
(14) Zhu, T.; Fu, C.; Xie, H.; Liu, Y.; Zhao, X. High efficiency half-Heusler thermoelectric materials for energy harvesting. *Adv. Energy Mater.* **2015**, *5*, No. 1500588.
(15) Dresselhaus, M. S.; Chen, G.; Tang, M. Y.; Yang, R.; Lee, H.; Wang, D.; Ren, Z.; Fleurial, J.-P.; Gogna, P. New directions for low-dimensional thermoelectric materials. *Adv. Mater.* **2007**, *19*, 1043−1053.
(16) Li, D.; Gong, Y.; Chen, Y.; Lin, J.; Khan, Q.; Zhang, Y.; Li, Y.; Zhang, H.; Xie, H. Recent progress of two-dimensional thermoelectric materials. *Nano-Micro Lett.* **2020**, *12*, No. 36.
(17) Sootsman, J. R.; Chung, D. Y.; Kanatzidis, M. G. New and old concepts in thermoelectric materials. *Angew. Chem., Int. Ed.* **2009**, *48*, 8616−8639.
(18) Biswas, K.; He, J.; Blum, I. D.; Wu, C. I.; Hogan, T. P.; Seidman, D. N.; Dravid, V. P.; Kanatzidis, M. G. High-performance bulk thermoelectrics with all-scale hierarchical architectures. *Nature* **2012**, *489*, 414−418.
(19) Zhao, L. D.; Tan, G.; Hao, S.; He, J.; Pei, Y.; Chi, H.; Wang, H.; Gong, S.; Xu, H.; Dravid, V. P.; et al. Ultrahigh power factor and thermoelectric performance in hole-doped single-crystal SnSe. *Science* **2016**, *351*, 141−144.
(20) Zhou, Z. Z.; Liu, H. J.; Fan, D. D.; Cao, G. H.; Sheng, C. Y. High thermoelectric performance in the hexagonal bilayer structure consisting of light boron and phosphorus elements. *Phys. Rev. B* **2019**, *99*, No. 085410.
(21) Naguib, M.; Mashtalir, O.; Carle, J.; Presser, V.; Lu, J.; Hultman, L.; Gogotsi, Y.; Barsoum, M. W. Two-dimensional transition metal carbides. *ACS Nano* **2012**, *6*, 1322−1331.
(22) Khazaei, M.; Arai, M.; Sasaki, T.; Estili, M.; Sakka, Y. Two-dimensional molybdenum carbides: potential thermoelectric materials of the MXene family. *Phys. Chem. Chem. Phys.* **2014**, *16*, 7841−7849.
(23) Sajjad, M.; Singh, N.; Sattar, S.; Wolf, S. De.; Schwingenschlögl, U. Ultralow lattice thermal conductivity and thermoelectric properties of monolayer Tl_2O. *ACS Appl. Energy Mater.* **2019**, *2*, 3004−3008.
(24) Özbal, G.; Senger, R. T.; Sevik, C.; Sevincli, H. Ballistic thermoelectric properties of monolayer semiconducting transition metal dichalcogenides and oxides. *Phys. Rev. B* **2019**, *100*, No. 085415.
(25) Huang, W.; Da, H.; Liang, G. Thermoelectric performance of MX_2 (M = Mo, W; X = S, Se) monolayers. *J. Appl. Phys.* **2013**, *113*, No. 104304.
(26) Bera, J.; Sahu, S. Strain induced valley degeneracy: A route to the enhancement of thermoelectric properties of monolayer WS_2. *RSC Adv.* **2019**, *9*, 25216−25224.
(27) Ding, G.; Gao, G. Y.; Huang, Z.; Zhang, W.; Yao, K. Thermoelectric properties of monolayer MSe_2 (M = Zr, Hf): low lattice thermal conductivity and a promising figure of merit. *Nanotechnology* **2016**, *27*, No. 375703.
(28) Bera, J.; Betal, A.; Sahu, S. Spin orbit coupling induced enhancement of thermoelectric performance of HfX_2 (X = S, Se) and its Janus monolayer. *J. Alloys Compd.* **2021**, *872*, No. 159704.
(29) Singh, D.; Ahuja, R. Enhanced optoelectronic and thermoelectric properties by intrinsic structural defects in monolayer HfS_2. *ACS Appl. Energy Mater.* **2019**, *2*, 6891−6903.
(30) Qin, D.; Ge, X. J.; Ding, G. Q.; Gao, G. Y.; Lv, J. T. Strain-induced thermoelectric performance enhancement of monolayer $ZrSe_2$. *RSC Adv.* **2017**, *7*, 47243−47250.
(31) Kresse, G.; Hafner, F. Ab Initio molecular dynamics for liquid metals. *Phys. Rev. B* **1993**, *47*, 558−561.
(32) Kresse, G.; Joubert, D. From ultrasoft pseudopotentials to the projector augmented-wave method. *Phys. Rev. B* **1999**, *59*, 1758−1775.
(33) Perdew, J. P.; Burke, K.; Ernzerhof, M. Generalized gradient approximation made simple. *Phys. Rev. Lett.* **1996**, *77*, 3865.
(34) Li, W.; Carrete, J.; Katcho, N. A.; Mingo, N. ShengBTE: A solver of the Boltzmann transport equation for phonons. *Comput. Phys. Commun.* **2014**, *185*, 1747−1758.
(35) Togo, A.; Oba, F.; Tanaka, I. First-Principles calculations of the ferroelastic transition between rutile-type and $CaCl_2$-type SiO_2 at high pressure. *Phys. Rev. B* **2008**, *78*, No. 134106.
(36) Chen, X.; Wang, D.; Liu, X.; Li, L.; Sanyal, B. Two-dimensional square-A_2B (A = Cu, Ag, Au, and B = S, Se): Auxetic semiconductors with high carrier mobilities and unusually low lattice thermal conductivities. *J. Phys. Chem. Lett.* **2020**, *11*, 2925−2933.
(37) Batsanov, S. S. Van der Waals Radii of elements. *Inorg. Mater.* **2001**, *37*, 871−885.
(38) Madsen, G. K. H.; Singh, D. J. BoltzTraP. A code for calculating band-structure dependent quantities. *Comput. Phys. Commun.* **2006**, *175*, 67−71.
(39) Takagi, S. I.; Toriumi, A.; Iwase, M.; Tango, H. On the universality of inversion layer mobility in Si MOSFET's: Part I-effects of substrate impurity concentration. *IEEE Trans. Electron Devices* **1994**, *41*, 2357−2362.
(40) Zhang, W. X.; Huang, Z. S.; Zhang, W. L.; Li, Y. R. Two-dimensional semiconductors with possible high room temperature mobility. *Nano Res.* **2014**, *7*, 1731−1737.
(41) Hodul, D. T.; Stacy, A. M. Anomalies in the properties of $Hf(S_{2-x}Te_x)_{1-y}$ and $Hf(Se_{2-x}Te_x)_{1-y}$ near the metal-insulator transition. *J. Solid State Chem.* **1984**, *54*, 438−446.
(42) Obeid, M. M.; Bafekry, A.; Rehman, S. Ur.; Nguyen, C. V. A type-II GaSe/HfS_2 van der Waals heterostructure as promising photocatalyst with high carrier mobility. *Appl. Surf. Sci.* **2020**, *534*, No. 147607.
(43) Faghihnasiri, M.; Ahmadi, A.; Alvankar Golpayegan, S.; Garosi Sharifabadi, S.; Ramazani, A. A first-principles study of nonlinear elastic behavior and anisotropic electronic properties of two-dimensional HfS_2. *Nanomaterials* **2020**, *10*, No. 446.
(44) Peng, J.; Najmaei, S.; Dubey, M.; Chung, P. W. Dominant ZA phonons and thermal carriers in HfS_2. *J. Appl. Phys.* **2019**, *126*, No. 164302.
(45) Gu, X.; Yang, R. Phonon transport in single-layer transition metal dichalcogenides: A first-principles study. *Appl. Phys. Lett.* **2014**, *105*, No. 131903.
(46) Jin, Z.; Liao, Q.; Fang, H.; Liu, Z.; Liu, W.; Ding, Z.; Luo, T.; Yang, N. A Revisit to high thermoelectric performance of single-layer MoS_2. *Sci. Rep.* **2015**, *5*, No. 18342.
(47) Han, D.; Yang, X.; Du, M.; Xin, G.; Zhang, J.; Wang, X.; Cheng, L. Improved thermoelectric properties of WS_2-WSe_2 phononic crystals: insights from first-principles calculations. *Nanoscale* **2021**, *13*, 7176−7192.
(48) Kaur, H.; Yadav, S.; Srivastava, A. K.; Singh, N.; Rath, S.; Schneider, J. J.; Sinha, O. P.; Srivastava, R. High-Yield Synthesis and Liquid-Exfoliation of Two-Dimensional Belt-Like Hafnium Disulphide. *Nano Res.* **2018**, *11*, 343−353.

https://doi.org/10.1021/acsomega.1c04286
ACS Omega 2021, 6, 29820−29829